



Cite this: *Green Chem.*, 2021, **23**, 1823

# Efficient visible-light-driven Suzuki coupling reaction over Co-doped BiOCl/Ce-doped Bi<sub>2</sub>O<sub>2</sub>CO<sub>3</sub> composites†

Dan-Xia Zhao, Guo-Ping Lu  and Chun Cai \*

Suzuki coupling reaction is a widely practiced protocol in organic synthesis for the formation of C–C bonds. The conventional process for this reaction usually involves high temperatures and noble metals. Hence, the development of a green, cost-effective photocatalytic system is an attractive and challenging strategy for the reaction. Here, we report a modified palladium-free Co-doped BiOCl/Ce-doped Bi<sub>2</sub>O<sub>2</sub>CO<sub>3</sub> (CBCB) composite, which shows high photocatalytic activity under white LED irradiation. At room temperature, an excellent yield (91%) of the desired cross-coupling product biphenyl was obtained in environmentally friendly solvents. Density functional calculations, together with the experimental results, show that the presence of Co and Ce ions results in the appearance of some impurity levels near the Fermi level of pure BiOCl and Bi<sub>2</sub>O<sub>2</sub>CO<sub>3</sub>, which decreases their forbidden bandwidth, thus ensuring higher light absorption and superior electronic conductivity. Moreover, the intimate interfacial contact between Co-doped BiOCl and Ce-doped Bi<sub>2</sub>O<sub>2</sub>CO<sub>3</sub> planes has a significant impact on the separation and transfer of photoinduced charge carriers, which ultimately leads to a remarkable increase in visible-light-driven photocatalytic activity.

Received 12th December 2020,  
Accepted 27th January 2021

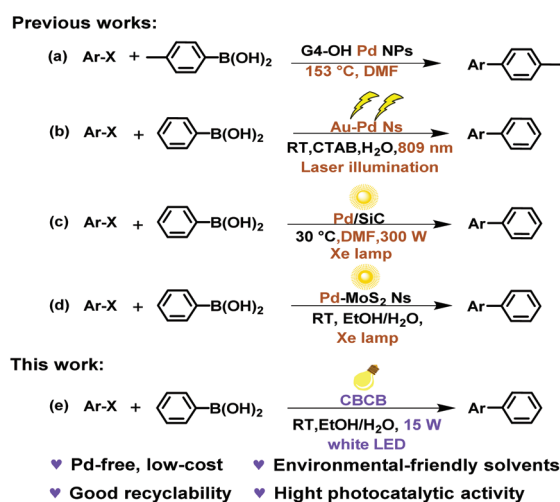
DOI: 10.1039/d0gc04206d

rsc.li/greenchem

## Introduction

Suzuki coupling of aryl halides with organoboron species is one of the most powerful tools in organic chemistry for the formation of C–C bonds.<sup>1–3</sup> Typically, Suzuki reactions are performed under homogeneous catalytic systems using a variety of Pd(II) or Pd(0) complexes.<sup>4,5</sup> Although typical homogeneous catalysts are highly efficient and selective, the recovery of potentially toxic palladium complexes and ligands is not in line with the development of green chemistry. In contrast, heterogeneous Pd catalysts are favored over homogeneous catalysts because of their ease of handling and reusability.<sup>6,7</sup> Nonetheless, many of these reported Suzuki coupling processes with heterogeneous catalysts are performed under heating conditions, which is energy intensive (Scheme 1a). Thus, visible light-driven Suzuki coupling reactions based on noble metal/semiconductor heterogeneous photocatalysis is a hot topic in the field of sustainable chemistry, because it combines catalytic efficiency and potential sunlight utilization.<sup>8</sup> Sun and co-workers studied the use of plasmonic Au–Pd nano-

structures as catalysts in Suzuki coupling reactions, and the yield obtained under illumination at 809 nm was ~2 times higher than that obtained for the reaction heated to the same temperature (Scheme 1b).<sup>9</sup> Apart from plasmonic metals, a high turnover frequency of 1053 h<sup>–1</sup> was reported for the Mott–Schottky type Pd/SiC heterojunction in the coupling of



**Scheme 1** Suzuki coupling reactions carried out under different heterogeneous catalysts.

Chemical Engineering College, Nanjing University of Science & Technology, 200 Xiaolingwei, Nanjing 210094, P. R. China. E-mail: c.cai@njust.edu.cn;  
Fax: +86-25-84315030; Tel: +86-25-84315514

† Electronic supplementary information (ESI) available: Complementary characterisation and catalytic data. See DOI: 10.1039/d0gc04206d

iodobenzene with phenylboronic acid under visible light irradiation at 30 °C (Scheme 1c).<sup>10</sup> Lim *et al.* showed that modification of MoS<sub>2</sub> nanosheets with Pd nanodots is an effective way to promote the Suzuki C–C coupling reaction under sunlight illumination at room temperature (Scheme 1d).<sup>11</sup>

Although supported palladium or other noble-metal-based catalysts show reasonable performance in C–C bond formation, their expensive price and scarce reserves limit their practical applications. Moreover, compared with their semiconductor counterparts, photocatalysts based on plasmonic metal nanoparticles show relatively low light absorption. Therefore, the development of a green and sustainable visible light active semiconductor photocatalyst based on non-noble metals is of high interest for both academia and research.

Bismuth-based materials are important visible-light-responsive photocatalysts and have generated a great deal of interest.<sup>12</sup> Among them, bismuth subcarbonate (Bi<sub>2</sub>O<sub>2</sub>CO<sub>3</sub>) and bismuth oxychloride (BiOCl) with a particular Sillen structure are Earth-abundant compounds with low toxicity.<sup>13</sup> Their inherent two-dimensional or three-dimensional layered crystal structure shows excellent photocatalytic activity due to its prolonged photocarrier lifetime and large specific surface area. Despite these advantages, several shortcomings, such as low visible light absorption ability and quantum efficiency, should be kept in mind. To address these issues, several strategies have recently attracted attention. Heteroatom doping is considered as an effective method because the electronic structure and implicitly the photocatalytic activity can be rationally controlled. For example, rare earth elements (Y,<sup>14</sup> Eu,<sup>15</sup> Er,<sup>16</sup> *etc.*) which have a 4f electron shell with a multi-electron configuration can act as shallow potential trapping centers for photo-generated electron–hole pairs. Therefore, doping with rare earth elements can prolong the separation time of carriers, thereby improving their photocatalytic activity.<sup>17</sup> Bi-based semiconductors doped with transition metal ions (Fe,<sup>18</sup> Cu,<sup>19</sup> Mn,<sup>20</sup> Zn,<sup>21</sup> *etc.*) exhibit a narrow bandgap and extended light absorption to the visible and even infrared light regions.<sup>20</sup> However, the formation of heterojunctions between Bi-based semiconductors and other materials could greatly influence their photocatalytic performance. Considering that BiOCl and Bi<sub>2</sub>O<sub>2</sub>CO<sub>3</sub> are similar in layered structure,<sup>22</sup> BiOCl/Bi<sub>2</sub>O<sub>2</sub>CO<sub>3</sub> composites have the advantage of easily matching the structure and forming heterostructures.<sup>23</sup> To our knowledge, this heterostructure has only been investigated for pollutant elimination. We were motivated to explore its application in photocatalytic Suzuki coupling reactions.

Herein, a Co-doped BiOCl/Ce-doped Bi<sub>2</sub>O<sub>2</sub>CO<sub>3</sub> (CBCB) heterojunction photocatalyst with a sphere-like morphology was successfully prepared by a simple hydrothermal method. The photocatalytic activity of the CBCB composite for the Suzuki coupling reaction between bromobenzene and phenylboronic acid was evaluated at room temperature and atmospheric pressure. As expected, an excellent yield (91%) of the desired product was obtained in environmentally friendly solvents (EtOH/H<sub>2</sub>O) under white LED irradiation (Scheme 1e). More

importantly, CBCB exhibits excellent recyclability, and can be reused at least five times without an obvious decrease of catalytic performance. We believe that this catalytic system meets the requirement of green chemistry. Furthermore, theoretical calculations and photoelectrochemical properties identified that doping heteroatoms in pure BiOCl and Bi<sub>2</sub>O<sub>2</sub>CO<sub>3</sub> phases can accelerate the separation of the interfacial electron–hole pairs, and the synergistic effect of favourable components in the two phases could be the key factor in improving the photocatalytic activity.

## Experimental section

### Synthesis of photocatalysts

A Co-doped BiOCl/Ce-doped Bi<sub>2</sub>O<sub>2</sub>CO<sub>3</sub> composite photocatalyst was synthesized by a solvothermal method, and it was labeled as CBCB (Scheme S1†). For comparison, the BiOCl/Bi<sub>2</sub>O<sub>2</sub>CO<sub>3</sub> composite was prepared according to the same procedure except for the precursor without cobalt and cerium ions and marked as BB. The detailed preparation methods of BiOCl, Bi<sub>2</sub>O<sub>2</sub>CO<sub>3</sub>, Co-doped BiOCl, Ce-doped Bi<sub>2</sub>O<sub>2</sub>CO<sub>3</sub>, BB and CBCB catalysts are provided in the ESI.†

### Characterization of photocatalysts

The as-prepared samples were characterized *via* X-ray powder diffraction (XRD), X-ray photoelectron spectroscopy (XPS), scanning electron microscopy (SEM), transmission electron microscopy (TEM)-X-ray spectroscopy (EDS), high-resolution transmission electron microscopy (HRTEM), UV-vis diffuse reflectance spectroscopy (DRS), photoluminescence (PL) spectroscopy, electrochemical impedance spectroscopy (EIS), and transient photocurrent response. Detailed information about experimental instruments and setting parameters is provided in the ESI.†

### Photocatalytic activity tests

For typical reactions, organohalides (0.2 mmol), boronic acids (0.22 mmol), K<sub>2</sub>CO<sub>3</sub> (0.45 mmol) and CBCB (25 mg) were added to 3 mL of EtOH/H<sub>2</sub>O (1:1) mixture in a glass vial under an argon atmosphere. The mixture was irradiated with a white LED lamp (15 W) for 16 h. The products were analyzed by GC-MS and GC.

### Theoretical calculation method

First-principles calculations within the framework of density functional theory (DFT) were performed by employing the Vienna *ab initio* simulation package (VASP). The computational details of calculation modes are provided in the ESI.†

## Results and discussion

### Characterization of samples

Fig. 1 shows the XRD patterns of different photocatalysts. The diffraction peaks of Bi<sub>2</sub>O<sub>2</sub>CO<sub>3</sub> and BiOCl can be indexed to

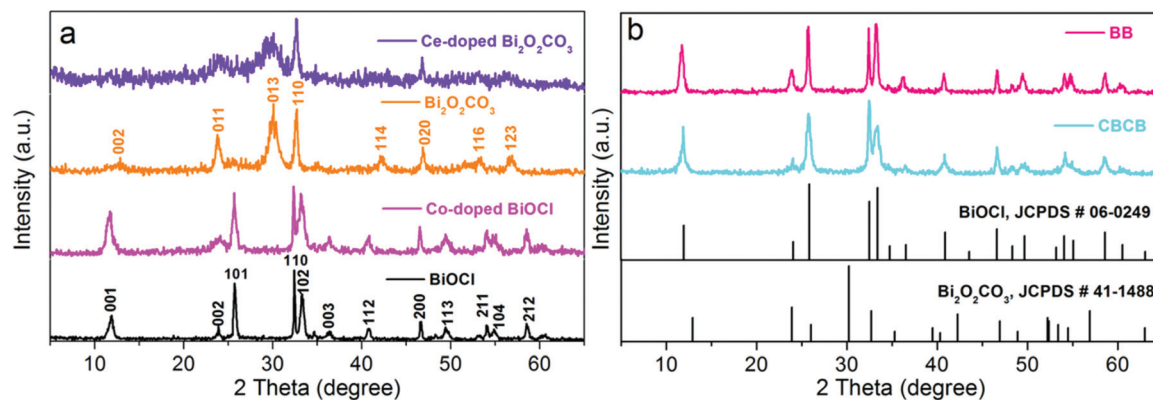


Fig. 1 XRD patterns of (a) BiOCl, Co-doped BiOCl, Bi<sub>2</sub>O<sub>2</sub>CO<sub>3</sub> and Ce-doped Bi<sub>2</sub>O<sub>2</sub>CO<sub>3</sub>; (b) BB and CBCB.

typical tetragonal Bi<sub>2</sub>O<sub>2</sub>CO<sub>3</sub> (JCPDS card No. 41-1488)<sup>24</sup> and BiOCl (JCPDS card No. 06-0249),<sup>25</sup> respectively. For Co-doped BiOCl and Ce-doped Bi<sub>2</sub>O<sub>2</sub>CO<sub>3</sub>, the sample still has the pure phase structure of BiOCl and Bi<sub>2</sub>O<sub>2</sub>CO<sub>3</sub>; no other compounds are observed, and the intensities of the diffraction peaks have become weaker, which is because the presence of metal ions affects the crystal size and limits the growth of the crystal in a specific lattice plane (Fig. 1a).<sup>26</sup> While for the BiOCl/Bi<sub>2</sub>O<sub>2</sub>CO<sub>3</sub> heterojunction, compared with the standard card, it can be seen that the peak of Bi<sub>2</sub>O<sub>2</sub>CO<sub>3</sub> or other compounds cannot be detected because the content of Bi<sub>2</sub>O<sub>2</sub>CO<sub>3</sub> is low and the high diffraction intensity of BiOCl covers the peak of Bi<sub>2</sub>O<sub>2</sub>CO<sub>3</sub> (Fig. 1b). Additionally, compared with pure BiOCl, an enhanced (102) peak emerged in the BiOCl/Bi<sub>2</sub>O<sub>2</sub>CO<sub>3</sub> (BB) phase. However, after the introduction of Co and Ce ions, the (002) and (003) peaks of CBCB became weaker and its (102) peak showed a small shift. The reason for such differences might be owing to the more intimate contact of the two phases of Co-doped BiOCl and Ce-doped Bi<sub>2</sub>O<sub>2</sub>CO<sub>3</sub> in the heterostructure vicinity.<sup>27</sup>

The morphologies of samples were analyzed by SEM. As shown in Fig. 2a, the pristine BiOCl is mainly composed of smooth nano-sheets with a size of 150–400 nm. The morphology of Co-doped BiOCl is similar to BiOCl, except that the nanosheets become rougher, and the size of Co-doped BiOCl remains in the range of 130–400 nm, indicating that the incorporation of metal Co ions has little effect on the morphology of Co-doped BiOCl (Fig. 2b). Bi<sub>2</sub>O<sub>2</sub>CO<sub>3</sub> (Fig. 2c) presents a large number of self-assembled flower-like microspheres with a width of 0.5–7 μm and a thickness of 20–70 nm, whereas Ce-doped Bi<sub>2</sub>O<sub>2</sub>CO<sub>3</sub> exhibits loose agglomerated micro-flowers with a smaller diameter, suggesting that the presence of Ce ions inhibits the growth and agglomeration process of Bi<sub>2</sub>O<sub>2</sub>CO<sub>3</sub> (Fig. 2d). The BB composite samples are regular nanosheets with thicknesses of 5–60 nm, and finally aggregated together to form flower-like microspheres (Fig. 2e).<sup>23</sup> After the coupling of Co-doped BiOCl and Ce-doped Bi<sub>2</sub>O<sub>2</sub>CO<sub>3</sub>, the size and thickness of the CBCB composite (Fig. 2f) become smaller and thinner compared to the BB composite. In the flower-like CBCB sample, the open pores formed by the inter-

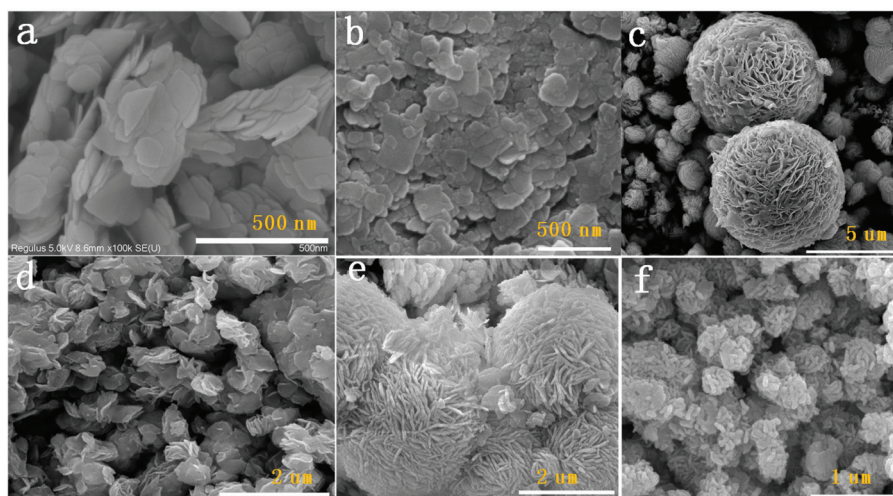


Fig. 2 SEM images of as-prepared samples: (a) BiOCl, (b) Co-doped BiOCl, (c) Bi<sub>2</sub>O<sub>2</sub>CO<sub>3</sub>, (d) Ce-doped Bi<sub>2</sub>O<sub>2</sub>CO<sub>3</sub>, (e) BB and (f) CBCB.

secting ultra-thin nanosheets allow the reactant to enter the inner surface of the photocatalyst and provide more active sites. Also, the open pores promote the multiple scattering of UV-vis light, thereby improving the light-harvesting ability.<sup>28</sup> The detailed microstructure of CBCB was further explored by TEM. Fig. 3a clearly shows that the size of the CBCB nanosheets is 0.15–0.5  $\mu\text{m}$  with an average thickness of about 20 nm. The Co-doped BiOCl nanosheets are well wrapped and infiltrated with Ce-doped  $\text{Bi}_2\text{O}_2\text{CO}_3$ , indicating that the two components are well coordinated in the heterojunction.<sup>29</sup> The HRTEM image in Fig. 3b exhibits the lattice orientation and heterojunction interface of CBCB. The clear lattice fringes of 0.275 nm and 0.273 nm are respectively ascribed to the (110) lattice planes of BiOCl and the (110) lattice planes of  $\text{Bi}_2\text{O}_2\text{CO}_3$ .<sup>30</sup> This result undoubtedly confirmed that the CBCB heterostructure has been successfully constructed as expected. Similarly, a clear heterojunction interface can also be seen in the TEM image of BB (Fig. 1S<sup>†</sup>). Furthermore, similar layered structures of Co-doped BiOCl and Ce-doped  $\text{Bi}_2\text{O}_2\text{CO}_3$  facilitate the formation of CBCB heterostructure nanocomposites. In the microspherical CBCB material, Ce-doped  $\text{Bi}_2\text{O}_2\text{CO}_3$  retains the original flower-like shape. Meanwhile, Ce-doped  $\text{Bi}_2\text{O}_2\text{CO}_3$  was used as a precursor, and then Co-doped BiOCl nanosheets were grown on the surface. It is conjectured that the interface contact layer between Co-doped BiOCl and Ce-doped  $\text{Bi}_2\text{O}_2\text{CO}_3$  nanosheets can be constructed through sharing the  $(\text{Bi}_2\text{O}_2)^{2-}$  sheets from  $\text{Bi}_2\text{O}_2\text{CO}_3$ .<sup>31</sup> In Scheme S1,<sup>†</sup> the possible growth mechanism of a heterojunction is proposed. The corresponding HAADF-STEM mode shows that Bi, Cl, O, C, Co, and Ce are well distributed in CBCB. Co and Ce elements are preferably located near the heterojunction interface, which proves that Co and Ce are successfully doped in the CBCB heterojunction photocatalyst (Fig. 3c).

The chemical state and elemental compositions of the CBCB composite were identified by XPS. As shown in

Fig. S2a,<sup>†</sup> it can be seen that Bi, Cl, O, C, Co, and Ce elements are all existing in the full survey spectrum, which is in agreement with the elemental mapping results. Two Bi peaks at 159.2 eV and 164.5 eV are ascribed to Bi 4f<sub>7/2</sub> and Bi 4f<sub>5/2</sub> from Bi<sup>3+</sup> ions in  $[\text{Bi}_2\text{O}_2]^{2+}$  (Fig. S2b<sup>†</sup>).<sup>32</sup> The O 1s spectra (Fig. S2c<sup>†</sup>) is mainly deconvoluted into three peaks with binding energies of 529.85, 531.17, and 532.3 eV, which can be assigned to the lattice oxygen of Bi–O, the surface hydroxyl groups, and chemisorbed oxygen, respectively.<sup>33</sup> In Fig. S2d,<sup>†</sup> the C has three chemical states, which are identified by the peaks at 284.8, 286.2, and 288.78 eV, respectively. The peak fitted at 284.8 eV comes from the standard reference carbon, while the peak observed at 286.2 and 288.6 eV should be ascribed to the C–O bond in  $[\text{CO}_3]^{2-}$ . The XPS signal of Cl 2p (Fig. S2e<sup>†</sup>) shows two major peaks around 197.9 and 199.5 eV, corresponding to Cl 2p<sub>3/2</sub> and Cl 2p<sub>1/2</sub> of Cl<sup>−</sup> in the CBCB sample, respectively.<sup>34</sup> The high-resolution Ce 3d spectrum is shown in Fig. S2f.<sup>†</sup> Multiple peaks between 880 eV and 915 eV indicate the co-existence of Ce<sup>3+</sup> and Ce<sup>4+</sup> in the CBCB nanocomposite. The peaks at 899.0 eV, 888.6 eV, and 881.6 eV are attributed to the 3d<sub>5/2</sub> level of Ce(IV), while the diffraction peaks at 906.6 eV and 902.2 eV are ascribed to the 3d<sub>3/2</sub> level of Ce(IV). The observed peaks at 903.9 and 885.5 eV belong to Ce(III).<sup>35,36</sup> In the spectrum of Co 2p, six peaks appear (Fig. S2g<sup>†</sup>), and the peaks at 778.1 and 795.3 eV are designated as Co<sup>0</sup> 2p<sub>3/2</sub> and Co<sup>0</sup> 2p<sub>1/2</sub>, respectively.<sup>37</sup> The binding energy of the Co 2p<sub>1/2</sub> peaks are located at 804.8 and 796.5 eV, and the Co 2p<sub>3/2</sub> peaks are observed at 781.2 and 780.3 eV, corresponding to the Co<sub>2</sub><sup>+</sup> species.<sup>38</sup> The strong interaction between Ce/Co elements and the composite accelerates the transfer of electrons between the interfaces, thereby greatly improving the photocatalytic activity of the nanocomposite.

UV-vis diffuse reflectance spectroscopy (DRS) is used to determine the optical properties of the as-prepared samples. As shown in Fig. 4,  $\text{Bi}_2\text{O}_2\text{CO}_3$  displays a sharp absorption edge

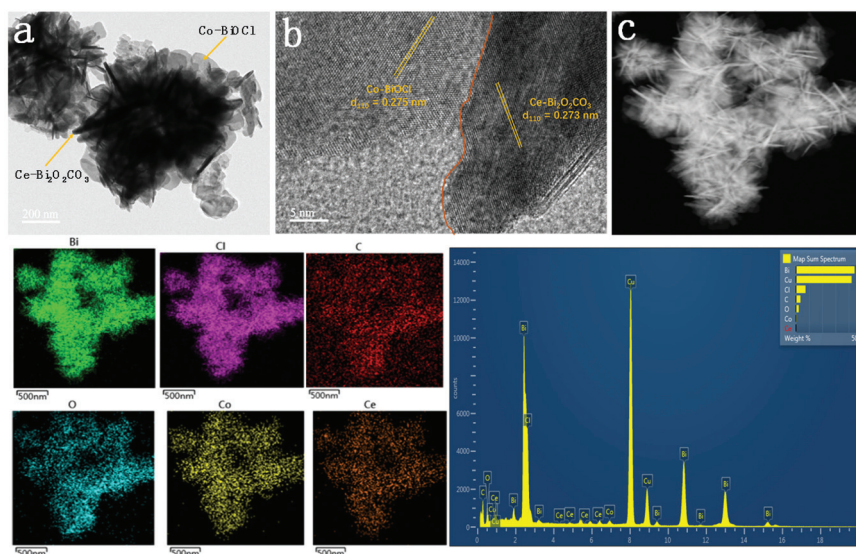


Fig. 3 (a) TEM and (b) HRTEM images of CBCB; (c) EDS elemental mapping images of Bi, Cl, C, O, Co and Ce elements.

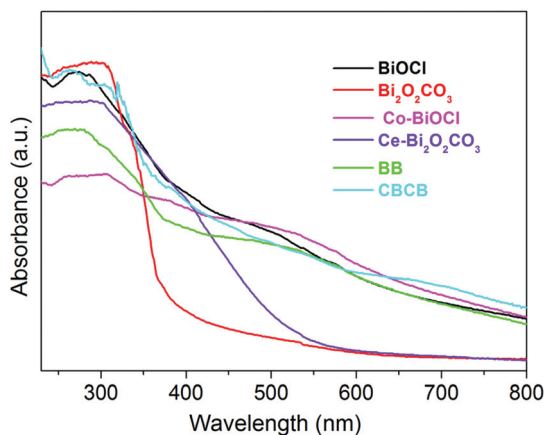


Fig. 4 UV-vis diffuse reflectance spectra of the samples.

of about 380 nm. The Ce-doped  $\text{Bi}_2\text{O}_2\text{CO}_3$  has a significant absorbance in the visible light region after introducing Ce to  $\text{Bi}_2\text{O}_2\text{CO}_3$ . Impressively, the absorption edge of BiOCl can extend to the visible light, almost covering the full solar spectrum. After anchoring Co@BiOCl, the absorbance of Co-doped BiOCl is enhanced in the range from 480 to 800 nm. Due to the essential bandgap absorption of BiOCl, both the BB and CBCB nanocomposites present similar absorption characteristics and induce a broad absorption in the visible light region. Therefore, it is reasonable that the heterojunction has more effective photocatalytic activity under visible light.<sup>39</sup> The bandgap of as-prepared photocatalysts can be calculated as follows:

$$\alpha h\nu = A (h\nu - E_g)^{n/2}$$

where  $\alpha$ ,  $h$ ,  $\nu$ ,  $E_g$ , and  $A$  are the absorption coefficient, Planck constant, light frequency, bandgap, and a constant, respectively. BiOCl and  $\text{Bi}_2\text{O}_2\text{CO}_3$  are indirect and direct semiconductors, respectively, and their corresponding  $n$  values are 4 and 2.<sup>30</sup> Hence, the bandgaps ( $E_g$ s) of BiOCl, Co-doped BiOCl,  $\text{Bi}_2\text{O}_2\text{CO}_3$ , and Ce-doped  $\text{Bi}_2\text{O}_2\text{CO}_3$  are 3.02, 2.81, 3.16,

and 2.90 eV, respectively (Fig. S3, ESI<sup>†</sup>). According to the evaluation of the XPS valence band (VB) spectrum, the VB potentials of BiOCl, Co-doped BiOCl,  $\text{Bi}_2\text{O}_2\text{CO}_3$ , and Ce-doped  $\text{Bi}_2\text{O}_2\text{CO}_3$  are approximately 2.80, 2.65, 1.70, and 2.24 V, respectively (Fig. S4, ESI<sup>†</sup>). The corresponding conduction-band (CB) potentials of samples are  $-0.22$ ,  $-0.16$ ,  $-1.46$ , and  $-0.66$  eV, respectively. The above results show that doping elements (Co and Ce) have a great influence on the band structure of BiOCl and  $\text{Bi}_2\text{O}_2\text{CO}_3$ .

### Photocatalytic Suzuki cross-coupling reaction

The photocatalytic activity of the synthesized materials (BiOCl, Co-doped BiOCl,  $\text{Bi}_2\text{O}_2\text{CO}_3$ , Ce-doped  $\text{Bi}_2\text{O}_2\text{CO}_3$ , BB and CBCB) was evaluated for the Suzuki coupling reaction between bromobenzene and phenylboronic acid at room temperature under visible light irradiation using a white LED lamp (15 W). As shown in Fig. 5a, among all as-prepared photocatalysts, the CBCB heterojunction photocatalyst exhibited the highest activity and achieved an excellent yield (91%) of the desired cross-coupling product, *i.e.*, biphenyl, with 16 h of reaction. Pure BiOCl and  $\text{Bi}_2\text{O}_2\text{CO}_3$  catalysts led to low yields of the coupling product. When the Co and Ce ions were inserted in the materials (Co-doped BiOCl and Ce-doped  $\text{Bi}_2\text{O}_2\text{CO}_3$  samples), the activity increased obviously, indicating that these catalysts can effectively activate the Suzuki coupling reaction of bromobenzene. In addition, compared with purely bismuth-based catalysts (*i.e.*, BiOCl, Co-doped BiOCl,  $\text{Bi}_2\text{O}_2\text{CO}_3$  and Ce-doped  $\text{Bi}_2\text{O}_2\text{CO}_3$ ), the yield of biphenyl products obtained by composite photocatalysts is higher. This indicates that the formed heterojunction can generate more effective light-excited electron-hole pairs to participate in the reaction. The control experiment performed in the dark showed that under identical experimental conditions, the yield for the coupling product was only 8% (Table 1, entry 2). No reaction was observed in the absence of a photocatalyst (Table 1, entry 3). Similarly, no biphenyl product in the absence of bromobenzene or phenylboronic acid could be found, indicating that there was no self-coupling phenomenon in the reaction (Table 1, entries 7 and 8).

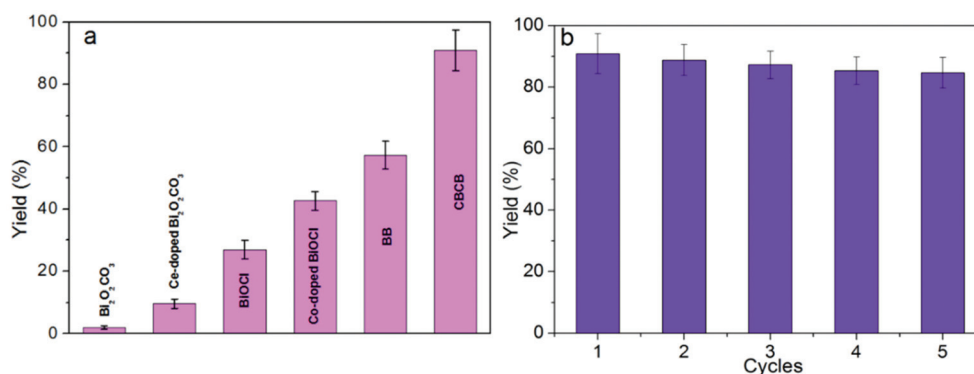
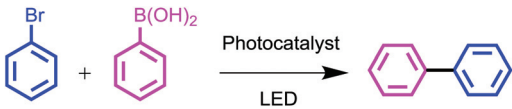


Fig. 5 (a) Photocatalytic activity of various catalysts under the same conditions. (b) Recycling ability of CBCB for a photocatalytic Suzuki coupling reaction. Reaction conditions: bromobenzene (0.2 mmol); phenylboronic acid (0.22 mmol);  $\text{K}_2\text{CO}_3$  (0.45 mmol); CBCB (25 mg); 1 : 1 EtOH/ $\text{H}_2\text{O}$ , 3 ml; RT; atmospheric pressure; 16 h; a 15 W white LED. Yields were determined by GC-MS and GC.

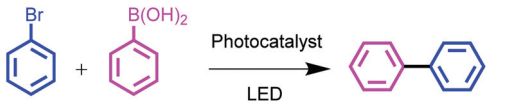
**Table 1** Screening and mechanistic study of the photocatalytic Suzuki coupling reaction using CBCB<sup>a</sup>


Entry	Reaction condition variations	Light	Yield <sup>b</sup> (%)
1	CBCB	+	91
2	CBCB	-	8
3	No CBCB	-	Trace
4	e <sup>-</sup> scavenger (BQ)	+	Trace
5	Hole scavenger (h <sup>+</sup> )	+	22
6	h <sup>+</sup> /e <sup>-</sup> /radical scavenger	+	Trace
7	No bromobenzene	+	Trace
8	No phenylboronic acid	+	Trace

<sup>a</sup> Reaction conditions: bromobenzene (0.2 mmol); phenylboronic acid (0.22 mmol); K<sub>2</sub>CO<sub>3</sub> (0.45 mmol); CBCB (25 mg); 1 : 1 EtOH/H<sub>2</sub>O, 3 ml; RT; atmospheric pressure; 16 h; a 15 W white LED. <sup>b</sup> Yield of the target product (mol %) was determined by GC-MS and GC analyses.

Compared with some reported reaction conditions of heterogeneous catalysts for Suzuki coupling (Tables S1 and 2†), it can be seen that both high temperatures and visible light drive the Suzuki coupling relying on various Pd-based catalysts. However, CBCB without Pd atoms can also achieve high conversion under mild conditions, indicating that the present work provides a sustainable approach for the formation of C–C bonds.

Under visible light irradiation, the effects of the different reaction conditions (solvents, bases, and reaction atmosphere) on the coupling reaction of bromobenzene with phenylboronic acid were investigated. First, the influence of several common solvents on the reaction results was studied. Polar aprotic solvents, such as *N,N*-dimethylformamide (DMF), dimethyl sulfoxide (DMSO), dioxane, and acetonitrile (ACN), were not appropriate for this reaction (Table 2, entries 11–14). The nonpolar solvent toluene led to a trace yield of product (Table 2, entry 15). By contrast, much higher yields were obtained in the polar protic solvents such as C<sub>2</sub>H<sub>5</sub>OH and H<sub>2</sub>O (Table 2, entries 9 and 10). These results are completely different from those usually obtained for conventional Suzuki reactions catalyzed by heterogeneous catalysts. Interestingly, a mixture of solvents led to a significant increase in photocatalytic activity. Hence, when EtOH–H<sub>2</sub>O (1 : 1) was used as the solvent, excellent biphenyl yield and selectivity were obtained (Table 2, entries 1, 4, 16 and 17), which is in line with the principles of green chemistry. The superior performance obtained in the mixed solvent can be attributed to the increase in the solubility of the reactants and bases. The bases dissolved in water can activate phenylboronic acid while enhancing the reaction rate in the aqueous medium.<sup>8</sup> In addition, compared with aprotic solvents, protic solvents may be oxidized more easily through photoinduced holes transferred from CBCB due to their lower oxidation potentials.<sup>40</sup> We also studied the influence of various bases (K<sub>2</sub>CO<sub>3</sub>, Cs<sub>2</sub>CO<sub>3</sub>, and Na<sub>2</sub>CO<sub>3</sub>) in a mixture of EtOH–H<sub>2</sub>O, K<sub>2</sub>CO<sub>3</sub> led to the best yield (Table 2, entry 1) while

**Table 2** Influence of the reaction conditions for Suzuki cross-coupling reactions<sup>a</sup>


Entry	Base	Solvent	Atmos	Yield <sup>b</sup> (%)
1	K <sub>2</sub> CO <sub>3</sub>	EtOH : H <sub>2</sub> O (1 : 1)	Ar	91
2	K <sub>2</sub> CO <sub>3</sub>	EtOH : H <sub>2</sub> O (1 : 1)	O <sub>2</sub>	8
3	K <sub>2</sub> CO <sub>3</sub>	EtOH : H <sub>2</sub> O (1 : 1)	Air	59
4	K <sub>2</sub> CO <sub>3</sub>	EtOH : H <sub>2</sub> O (2 : 1)	Ar	30
5	Cs <sub>2</sub> CO <sub>3</sub>	EtOH : H <sub>2</sub> O (1 : 1)	Ar	79
6	Na <sub>2</sub> CO <sub>3</sub>	EtOH : H <sub>2</sub> O (1 : 1)	Ar	43
7	KOH	EtOH : H <sub>2</sub> O (1 : 1)	Ar	30
8	NaOH	EtOH : H <sub>2</sub> O (1 : 1)	Ar	25
9	K <sub>2</sub> CO <sub>3</sub>	EtOH	Ar	39
10	K <sub>2</sub> CO <sub>3</sub>	H <sub>2</sub> O	Ar	28
11	K <sub>2</sub> CO <sub>3</sub>	DMF	Ar	11
12	K <sub>2</sub> CO <sub>3</sub>	DMSO	Ar	Trace
13	K <sub>2</sub> CO <sub>3</sub>	Dioxane	Ar	Trace
14	K <sub>2</sub> CO <sub>3</sub>	Acetonitrile	Ar	Trace
15	K <sub>2</sub> CO <sub>3</sub>	Toluene	Ar	Trace
16	K <sub>2</sub> CO <sub>3</sub>	DMF : H <sub>2</sub> O	Ar	30
17	K <sub>2</sub> CO <sub>3</sub>	DMSO : H <sub>2</sub> O	Ar	8

<sup>a</sup> Reaction conditions: bromobenzene (0.2 mmol); phenylboronic acid (0.22 mmol); K<sub>2</sub>CO<sub>3</sub> (0.45 mmol); CBCB (25 mg); 1 : 1 EtOH/H<sub>2</sub>O, 3 ml; RT; atmospheric pressure; 16 h; a 15 W white LED. <sup>b</sup> Yields were determined by GC-MS.

Cs<sub>2</sub>CO<sub>3</sub> showed good activity for the Suzuki coupling reaction (Table 2, entry 5). However, Na<sub>2</sub>CO<sub>3</sub> and hydroxides (KOH and NaOH) led to relatively low selectivities and yield of the desired product (Table 2, entries 6–8). Moreover, without the protection of an inert gas, the yield of the corresponding product is significantly reduced (Table 2, entries 1–3).

After the optimization studies, the photocatalytic Suzuki coupling reaction was performed for different substrates (Table S3†). Good yields of biphenyl could be obtained by coupling various aryl halides with arylboronic acids (Table S3, entries 1–3†). As expected, bromobenzene with electron-donating groups (*i.e.*, CH<sub>3</sub>, NH<sub>2</sub>, and OH, see entries 4–6) exhibited lower product yields, as compared to those with electron-withdrawing groups (*i.e.*, Cl and F). Phenylboronic acid with electron-donating substituents (Table S3, entries 7 and 10†) exhibited a higher reactivity than those with electron-withdrawing ones (Table S3, entry 11†). Moreover, steric hindrance had a negative impact on the coupling reaction and the *ortho*-substituted substrates leading to relatively low yields (Table S3, entries 7–9†).

To elucidate the electron transfer mechanism in the photocatalyzed Suzuki cross-coupling reactions, the coupling of bromobenzene and phenylboronic acid in the presence of electron and hole scavengers was studied. *p*-Benzoquinone (BQ) was used as an electron scavenger to trap photoinduced electrons on the surface of the catalyst. Therefore, the use of 0.4 mmol BQ resulted in only trace amounts of product, highlighting the key role played by the electrons in this reaction (Table 1, entry 4). Triethanolamine (TEA) is a well-known hole scavenger. Yet, when 0.4 mmol TEA was added, the yield of the desired biphenyl

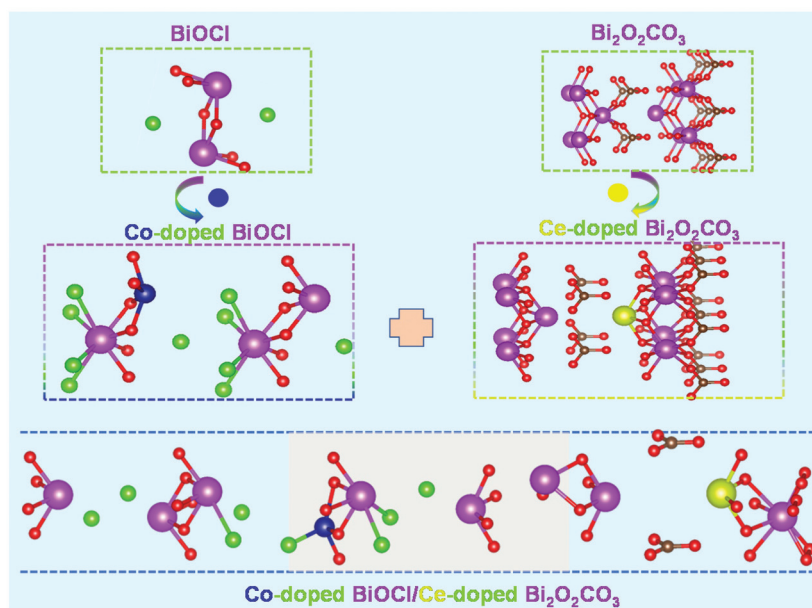


Fig. 6 Atomic-layer stacking of a BiOCl, Bi<sub>2</sub>O<sub>2</sub>CO<sub>3</sub>, Co-doped BiOCl, Ce-doped Bi<sub>2</sub>O<sub>2</sub>CO<sub>3</sub> and Co-doped BiOCl (001)/Ce-doped Bi<sub>2</sub>O<sub>2</sub>CO<sub>3</sub> (001) heterojunction model. Green, purple, red, brown, blue and yellow atoms are Cl, Bi, O, C, Co and Ce, respectively.

decreased to 22% (Table 1, entry 5). We speculate that the photo-generated holes can diffuse into the adsorption sites of phenylboronic acid, and the adsorbed molecules could be oxidized with the cleavage of the C–B bond.<sup>40,41</sup> Moreover, the strong paramagnetic resonance (EPR) signal at a *g* value of 2.0 was detected on the CBCB (Fig. S5<sup>†</sup>), indicating that oxygen vacancies were generated in CBCB.<sup>42</sup> Although these results suggest the importance of the electron–hole pairs in the photocatalytic Suzuki reaction, the exact role of holes remains unclear.

The reusability of the CBCB photocatalyst was investigated to evaluate the stability of the designed architecture. After the photocatalytic Suzuki coupling, the CBCB photocatalyst was separated from the reaction solution by centrifugation. Afterwards, it was used in a new catalytic cycle under identical conditions. As shown in Fig. 5b, the recovered photocatalyst exhibited high catalytic performance for the five cycles without obvious loss of activity. Furthermore, the inductively coupled plasma mass spectrometry (ICP-MS) test shows that the content of Co/Ce in CBCB remains above 0.95%/0.2% after photocatalysis (Table S4<sup>†</sup>). There is no significant change in the crystalline structure and morphology of the recovered catalyst observed through XRD and SEM, respectively (Fig. S6<sup>†</sup>). From the HRTEM image of the recovered photocatalyst, a clear heterojunction interface can be observed, which further proves that there exists intimate interfacial contact between Co-doped BiOCl and Ce-doped Bi<sub>2</sub>O<sub>2</sub>CO<sub>3</sub> planes (Fig. S7<sup>†</sup>). These results demonstrate that CBCB exhibited good stability and was suitable as a photocatalyst for Suzuki coupling reactions.

### Theoretical exploration

Based on the first-principles calculation of the crystal structure properties, the energy band structure, and the density of

states, the mechanism using CBCB as an efficient photocatalyst in the coupling reaction was explored. Fig. 6 shows the atomic models of bulk BiOCl, Bi<sub>2</sub>O<sub>2</sub>CO<sub>3</sub>, Co-doped BiOCl, and Ce-doped Bi<sub>2</sub>O<sub>2</sub>CO<sub>3</sub> structures. The lattice constants were found to be *a* = *b* = 3.917 Å and *c* = 7.408 Å for BiOCl and *a* = 4.014 Å, *b* = 4.011 Å, and *c* = 14.204 Å for Bi<sub>2</sub>O<sub>2</sub>CO<sub>3</sub>, which are consistent with the experimental values.<sup>43,44</sup> When doped with metal ions (Ce or Co), the lattice parameters of BiOCl are *a* = *b* = 3.83 Å and *c* = 7.244 Å. For Bi<sub>2</sub>O<sub>2</sub>CO<sub>3</sub>, the lattice constants are *a* = 4.033 Å, *b* = 4.029 Å, and *c* = 14.28 Å. The interface model employed the average size of both BiOCl and Bi<sub>2</sub>O<sub>2</sub>CO<sub>3</sub> slabs to make a small mismatch (~0.50%) along the *a*- and *b*-axis. Experimentally, the Co-doped BiOCl (001) and Ce-doped Bi<sub>2</sub>O<sub>2</sub>CO<sub>3</sub> (001) facets will generate plenty of oxygen vacancies under UV/visible light. These oxygen vacancies increase the separation efficiency of carriers, resulting in the (001) crystal planes of BiOCl and Bi<sub>2</sub>O<sub>2</sub>CO<sub>3</sub> exhibiting excellent photoactivity.<sup>45–47</sup> Therefore, it would be beneficial to construct a heterojunction model by contacting the BiOCl (001) plane and the Bi<sub>2</sub>O<sub>2</sub>CO<sub>3</sub> (001) plane.

To explore the interaction between the components in the CBCB heterojunction, we analyzed their electronic structure. As shown in Fig. S8a,<sup>†</sup> the bandgaps of pure BiOCl and Bi<sub>2</sub>O<sub>2</sub>CO<sub>3</sub> are 2.5 and 0.3 eV, respectively, which are smaller than the experimental value. This phenomenon stems from the limitation of DFT calculations; the discontinuity of the exchange-related potential is not considered in the DFT framework.<sup>48</sup> Compared with bulk BiOCl, after Co ion doping, some impurity levels appear near the Fermi level of BiOCl, which reduces the bandgap of Co-doped BiOCl to 1.6 eV. Fig. 7a shows that the impurity energy level mainly appears near the top of the valence band, indicating that Co-doped BiOCl is a p-type semi-

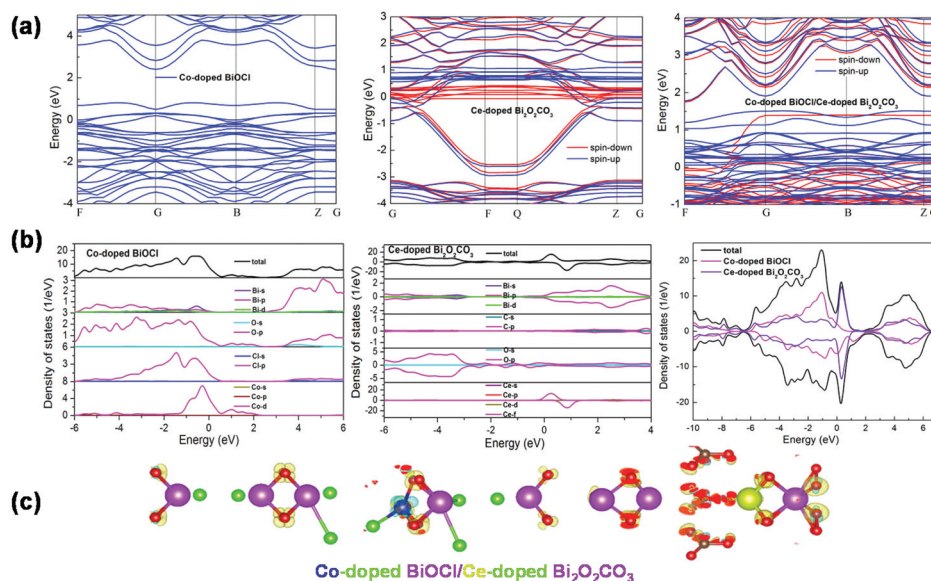


**Fig. 7** (a) Band structures, and (b) total density of states and local density of states of Co-doped BiOCl, Ce-doped Bi<sub>2</sub>O<sub>2</sub>CO<sub>3</sub> and a Co-doped BiOCl (001)/Ce-doped Bi<sub>2</sub>O<sub>2</sub>CO<sub>3</sub> (001) heterojunction model. The positive DOS is for spin up while the negative one is for spin down. (c) The electron difference density maps of the Co-doped BiOCl (001)/Ce-doped Bi<sub>2</sub>O<sub>2</sub>CO<sub>3</sub> (001) interface. Green, purple, red, brown, blue and yellow atoms are Cl, Bi, O, C, Co and Ce, respectively.

conductor. With the addition of Co ions, BiOCl and the Co elements are likely to form a homogenous junction locally, and the built-in electric field formed in the Co-doped BiOCl can effectively separate the photoinduced carriers generated by BiOCl, thus greatly enhancing the photocatalytic activity of BiOCl. As shown in Fig. 7a, Ce is embedded in Bi<sub>2</sub>O<sub>2</sub>CO<sub>3</sub> with a spin state. There are two spin states near the Fermi level of Ce-doped Bi<sub>2</sub>O<sub>2</sub>CO<sub>3</sub>, and the bandgap value of the spin-down part is close to 0, making the system exhibit metallic characteristics. Due to the presence of Ce-doped Bi<sub>2</sub>O<sub>2</sub>CO<sub>3</sub>, the band structure of the CBCB heterojunction also presents a spin state. Compared to pure Co-doped BiOCl and Ce-doped Bi<sub>2</sub>O<sub>2</sub>CO<sub>3</sub>, the impurity energy level of CBCB near the Fermi level increases significantly and becomes denser, indicating the enhancement of hybridization between Co-doped BiOCl and Ce-doped Bi<sub>2</sub>O<sub>2</sub>CO<sub>3</sub>, which is conducive to charge transfer at the interface.

To explain the change in the energy band from a microscopic point of view, the density of states of different samples was calculated and analyzed. It can be seen from Fig. S8b† that the valence band maximum (VBM) of bulk BiOCl is mainly determined by the O 2p and Cl 3p states, while the Bi 6s and Bi 6p state contribution is small. The conduction band minimum (CBM) is mostly dominated by the Bi 6p states. After Co atom doping, the VBM at the Fermi level is mainly provided by the Cl 3p and Co 3d states, and the CBM is mainly contributed by the Bi 6p states (Fig. 7b). Moreover, resonance hybridization occurs near the Fermi level of BiOCl, causing the electrons there to be more active. The formed intermediate energy level greatly reduces the forbidden bandwidth, thereby making the optical excitation easier and generating more charge carriers. For bulk Bi<sub>2</sub>O<sub>2</sub>CO<sub>3</sub>, the VBM of Bi<sub>2</sub>O<sub>2</sub>CO<sub>3</sub> is

mainly composed of O 2p orbitals in the CO<sub>3</sub><sup>2-</sup> layer, and the CBM is mainly composed of Bi 6p orbitals in the Bi<sub>2</sub>O<sub>2</sub><sup>2+</sup> layer (Fig. S8b†). The electron transition mode excited by light is O 2p → Bi 6p. The doping of the Ce ions greatly affects the total density of states (TDOS) and the local density of states (LDOS) of Bi<sub>2</sub>O<sub>2</sub>CO<sub>3</sub>, and the system shows the spin-polarized DOS. The VBM of Ce-doped Bi<sub>2</sub>O<sub>2</sub>CO<sub>3</sub> is still mainly determined by O 2p orbitals; while the CBM is mostly contributed by Bi 6p and Ce 4f orbitals, of which Ce 4f orbitals account for a larger proportion (Fig. 7b). Additionally, it can be observed that the 4f orbital of Ce crosses the Fermi level, that is, the 4f orbital of Ce appears at the bottom of the CB and the top of the VB. The main reason for this phenomenon is that it has two valence states of Ce<sup>4+</sup> and Ce<sup>3+</sup> (see the analysis of XPS in Fig. S2†). Ce<sup>4+</sup> easily captures photogenerated electrons and prevents the recombination of electron-hole pairs, thus improving the catalytic activity of Bi<sub>2</sub>O<sub>2</sub>CO<sub>3</sub>. Consistent with the analysis results of the above band structure, the existence of Ce-doped Bi<sub>2</sub>O<sub>2</sub>CO<sub>3</sub> makes CBCB exhibit a spin-polarized total density of states (TDOS). The Ce oxidation state (+3 or +4) in the CBCB composite significantly affects the spin state, which in turn may regulate the photocatalytic performance.<sup>49</sup> Moreover, the coupling of Co-doped BiOCl and Ce-doped Bi<sub>2</sub>O<sub>2</sub>CO<sub>3</sub> showed an increased charge density near the Fermi level. Therefore, we speculated that the CBCB heterojunction will exhibit enhanced photoresponsivity.<sup>50</sup> On the other hand, the charge in the heterojunction CBM is mostly localized on Ce-doped Bi<sub>2</sub>O<sub>2</sub>CO<sub>3</sub>, and the charge in the VBM is mainly localized on Co-doped BiOCl, indicating that CBCB is a type II heterojunction. The VBM and CBM states are located in different components of the CBCB heterostructure, which can realize the

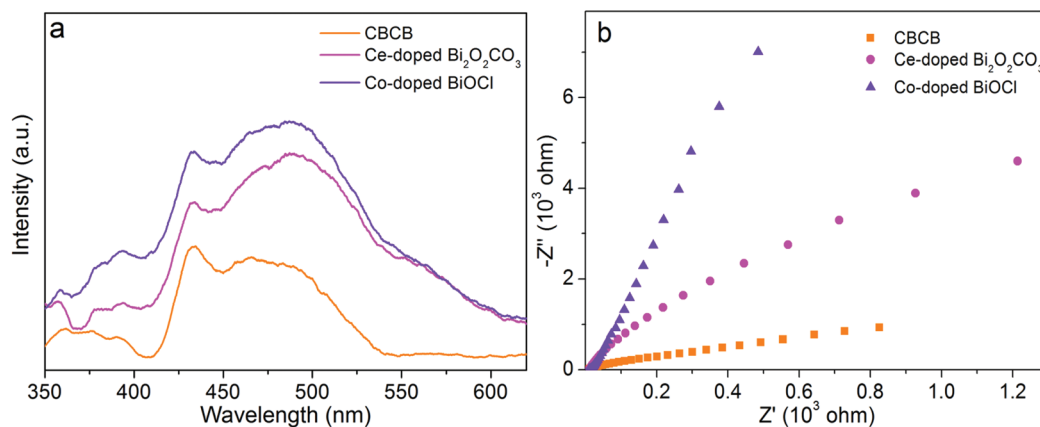


Fig. 8 Photoluminescence (a) and EIS-Nyquist plots (b) of Co-doped BiOCl, Ce-doped Bi<sub>2</sub>O<sub>2</sub>CO<sub>3</sub> and a Co-doped BiOCl/Ce-doped Bi<sub>2</sub>O<sub>2</sub>CO<sub>3</sub> heterojunction.

effective separation of electrons and holes in space, and improve the photocatalytic performance of the photocatalyst.

The electron difference density and Bader charge analyses are used to investigate the charge transfer of the CBCB interface. In Fig. 7c, the yellow and blue regions represent charge accumulation and depletion, respectively. For the Co-doped BiOCl layer, part of the electrons of Co atoms are transferred to the BiOCl phase, resulting in the formation of a built-in electric field in Co-doped BiOCl, which is in line with the energy band analysis. Compared with Co-doped BiOCl, Ce-doped Bi<sub>2</sub>O<sub>2</sub>CO<sub>3</sub> accumulates more charges on the surface. When a heterojunction is formed between Co-doped BiOCl and Ce-doped Bi<sub>2</sub>O<sub>2</sub>CO<sub>3</sub>, charge shift and redistribution will occur at the interface of the heterojunction, indicating a strong interaction between the two components.<sup>51</sup> Meanwhile, Bader charge analysis found that the charge flows from the Ce-doped Bi<sub>2</sub>O<sub>2</sub>CO<sub>3</sub> layer to the Co-doped BiOCl layer (0.2 e), which following our expected experimental results.

To further investigate the separation efficiency of the photo-generated charge carriers of catalysts, the PL spectra were recorded (Fig. 8a). Clearly, compared with Co-doped BiOCl and Ce-doped Bi<sub>2</sub>O<sub>2</sub>CO<sub>3</sub>, the PL signal intensity of hybrid CBCB was suppressed. That is, under visible light irradiation, the electrons migrate from the LUMO of Ce-doped Bi<sub>2</sub>O<sub>2</sub>CO<sub>3</sub> to the conduction band (CB) of Co-doped BiOCl, and Ce<sup>4+</sup> can also act as the electron capture trap, leading to the spatial separation of charge carriers,<sup>27</sup> and thus delaying the electron-hole pair recombination. The result is in good agreement with the above theoretical calculation. The electron transfer mechanism of the photocatalyst was also studied through transient photocurrent and EIS experiments. As expected, Co-doped BiOCl and Ce-doped Bi<sub>2</sub>O<sub>2</sub>CO<sub>3</sub> exhibited a lower photocurrent density. However, when the Co-doped BiOCl and Ce-doped Bi<sub>2</sub>O<sub>2</sub>CO<sub>3</sub> formed a heterojunction, the photocurrent density of CBCB increased remarkably, indicating that more photo-generated electrons in the composite were transferred to ITO (Fig. S9†). The EIS spectrum of the prepared samples is shown in Fig. 8b. Similar to the results of PL analysis, the arc radius

of CBCB is relatively small, indicating a faster interface charge transfer of the heterojunction photocatalyst.

### Mechanism

Unlike the homogeneous catalysts used for the Suzuki coupling reaction for which the mechanism is easier to establish, for a heterogeneous catalyst with multiple active sites, the mechanism is difficult to understand. On the basis of the previously reported works, DFT calculations, and experimental results obtained herein, the photocatalytic mechanism of the Suzuki coupling reaction over CBCB hybrids under visible light irradiation was proposed (Fig. 9). Upon light irradiation, the photocatalyst CBCB can absorb a part of the visible light, generating electron-hole pairs in Co-doped BiOCl and Ce-doped Bi<sub>2</sub>O<sub>2</sub>CO<sub>3</sub> layers. Due to the intimate interfacial contact between the Co-doped BiOCl and Ce-doped Bi<sub>2</sub>O<sub>2</sub>CO<sub>3</sub>, the electrons in the conduction band of Ce-doped Bi<sub>2</sub>O<sub>2</sub>CO<sub>3</sub> are easily transferred to the conduction band of Co-doped BiOCl, which activates the C-X bond of the aryl halides and reduces it to the corresponding aryl anion radical.<sup>40,52</sup> Simultaneously, the holes in the valence band of Co-doped BiOCl migrate to the valence band of Ce-doped Bi<sub>2</sub>O<sub>2</sub>CO<sub>3</sub>, and the photogenerated holes activate the C-B bond of phenylboronic acid. Phenylboronic acid captures OH<sup>-</sup> from the alkaline reaction medium to produce B(OH)<sup>3-</sup>, which is then converted into a phenyl radical cation with the assistance of photoinduced holes.<sup>53</sup> Finally, the phenyl radical cation and aryl anion undergo a cross-coupling reaction to obtain the desired biphenyl product. On the other hand, compared to the heterojunction constructed from BiOCl and Bi<sub>2</sub>O<sub>2</sub>CO<sub>3</sub>, the heterojunction interface made of Co-doped BiOCl and Ce-doped Bi<sub>2</sub>O<sub>2</sub>CO<sub>3</sub> can effectively shorten the diffusion length of charge carriers and improve the transmission efficiency of electron-hole pairs. All these results indicate that the introduction of Co and Ce ions and the construction of a Co-doped BiOCl/Ce-doped Bi<sub>2</sub>O<sub>2</sub>CO<sub>3</sub> heterojunction can significantly inhibit the recombination of photoinduced charge carriers and enhance the photocatalytic activity of the Suzuki cross-coupling reaction.

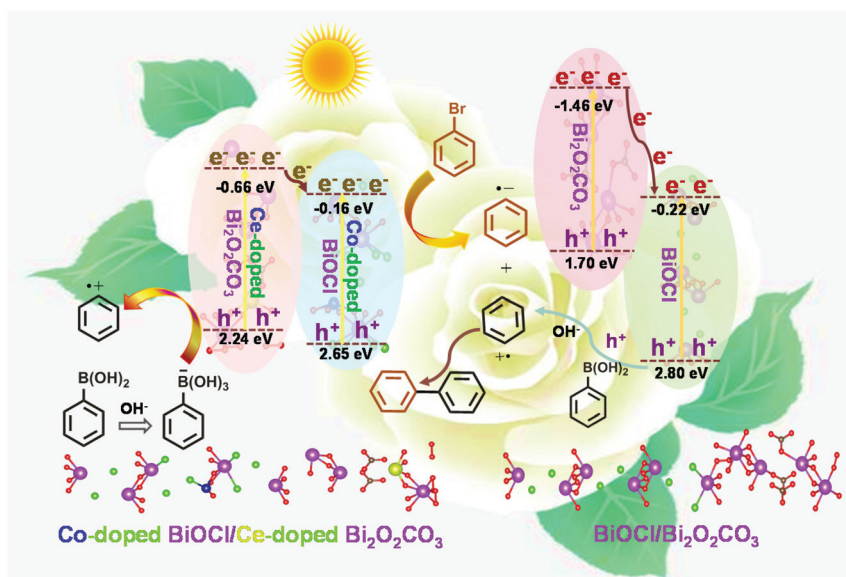


Fig. 9 Proposed mechanism of the photocatalytic Suzuki cross-coupling of bromobenzene and phenylboronic acid.

## Conclusions

In summary, a modified BiOCl/Bi<sub>2</sub>O<sub>2</sub>CO<sub>3</sub> (CBCB) composite was successfully prepared, which acts as a highly efficient palladium-free heterogeneous photocatalyst for the Suzuki coupling reaction. As expected, an excellent yield (91%) of the desired product biphenyl was obtained under mild conditions. The highly efficient photocatalytic performance over CBCB can be attributed to the following points: (1) the incorporation of Co ions makes Co-doped BiOCl exhibit a narrowed bandgap and enhances the light absorption. Moreover, a built-in electric field directed from Co to BiOCl is formed in the Co-doped BiOCl layer, resulting in an accelerated charge transfer process; (2) when Bi<sub>2</sub>O<sub>2</sub>CO<sub>3</sub> is doped with Ce, the low-lying empty 4f orbital of Ce<sup>4+</sup> easily captures light-excited electrons, thereby preventing the recombination of electron-hole pairs. On the other hand, the spin state of Ce in Ce-doped Bi<sub>2</sub>O<sub>2</sub>CO<sub>3</sub> can greatly regulate the photocatalytic performance; and (3) the type II heterojunction constructed by the Co-doped BiOCl and Ce-doped Bi<sub>2</sub>O<sub>2</sub>CO<sub>3</sub> facets effectively promotes the separation and transfer of photogenerated electron-hole pairs due to intimate interfacial contact and appropriate energy level positions. Thus, the utilization of visible light as the energy source, EtOH/H<sub>2</sub>O as environmentally friendly solvents, high photocatalytic activity and reusability is expected to make the modified palladium-free BiOCl/Bi<sub>2</sub>O<sub>2</sub>CO<sub>3</sub> composite a promising greener energy environmental material.

## Conflicts of interest

There are no conflicts to declare.

## Acknowledgements

We gratefully acknowledge the Key Laboratory of Biomass Energy and Material, Jiangsu Province (JSBEM201912) and the Chinese Postdoctoral Science Foundation (2015 M571761 and 2016T90465) for financial support. This work was funded by the Priority Academic Program Development of Jiangsu Higher Education Institution and Instrument and Equipment Foundation of Nanjing University of Science & Technology.

## Notes and references

- N. Miyaura and A. Suzuki, *J. Chem. Soc., Chem. Commun.*, 1979, 866–867, DOI: 10.1039/C39790000866.
- A. Suzuki, *Angew. Chem., Int. Ed.*, 2011, **50**, 6722–6737.
- Á. Molnár, *Chem. Rev.*, 2011, **111**, 2251–2320.
- S.-Y. Ding, J. Gao, Q. Wang, Y. Zhang, W.-G. Song, C.-Y. Su and W. Wang, *J. Am. Chem. Soc.*, 2011, **133**, 19816–19822.
- N. T. S. Phan, M. Van Der Sluys and C. W. Jones, *Adv. Synth. Catal.*, 2006, **348**, 609–679.
- M. Pittelkow, K. Moth-Poulsen, U. Boas and J. B. Christensen, *Langmuir*, 2003, **19**, 7682–7684.
- P. Slavík, D. W. Kurka and D. K. Smith, *Chem. Sci.*, 2018, **9**, 8673–8681.
- Q. Xiao, S. Sarina, E. Jaatinen, J. Jia, D. P. Arnold, H. Liu and H. Zhu, *Green Chem.*, 2014, **16**, 4272–4285.
- F. Wang, C. Li, H. Chen, R. Jiang, L.-D. Sun, Q. Li, J. Wang, J. C. Yu and C.-H. Yan, *J. Am. Chem. Soc.*, 2013, **135**, 5588–5601.
- Z. Jiao, Z. Zhai, X. Guo and X.-Y. Guo, *J. Phys. Chem. C*, 2015, **119**, 3238–3243.

- 11 H. H. Shin, E. Kang, H. Park, T. Han, C.-H. Lee and D.-K. Lim, *J. Mater. Chem. A*, 2017, **5**, 24965–24971.
- 12 R. He, D. Xu, B. Cheng, J. Yu and W. Ho, *Nanoscale Horiz.*, 2018, **3**, 464–504.
- 13 Y. Huang, K. Li, Y. Lin, Y. Tong and H. Liu, *ChemCatChem*, 2018, **10**, 1982–1987.
- 14 M. He, W. Li, J. Xia, L. Xu, J. Di, H. Xu, S. Yin, H. Li and M. Li, *Appl. Surf. Sci.*, 2015, **331**, 170–178.
- 15 A. Dash, S. Sarkar, V. N. K. B. Adusumalli and V. Mahalingam, *Langmuir*, 2014, **30**, 1401–1409.
- 16 J. Xia, M. Ji, W. Li, J. Di, H. Xu, M. He, Q. Zhang and H. Li, *Colloids Surf., A*, 2016, **489**, 343–350.
- 17 J. Di, J. Xia, H. Li, S. Guo and S. Dai, *Nano Energy*, 2017, **41**, 172–192.
- 18 Y. Mi, L. Wen, Z. Wang, D. Cao, R. Xu, Y. Fang, Y. Zhou and Y. Lei, *Nano Energy*, 2016, **30**, 109–117.
- 19 X. Gao, J. Fei, Y. Dai and F. Fu, *J. Mol. Liq.*, 2018, **256**, 267–276.
- 20 X. Zhang, C. Fan, Y. Wang, Y. Wang, Z. Liang and P. Han, *Comput. Mater. Sci.*, 2013, **71**, 135–145.
- 21 W. T. Li, W. Z. Huang, H. Zhou, H. Y. Yin, Y. F. Zheng and X. C. Song, *J. Alloys Compd.*, 2015, **638**, 148–154.
- 22 S. Fang, C. Ding, Q. Liang, Z. Li, S. Xu, Y. Peng and D. Lu, *J. Alloys Compd.*, 2016, **684**, 230–236.
- 23 J. Xie, N. Guo, A. Liu, Y. Cao, J. Hu and D. Jia, *J. Alloys Compd.*, 2019, **784**, 377–385.
- 24 S. Yu, Y. Zhang, F. Dong, M. Li, T. Zhang and H. Huang, *Appl. Catal., B*, 2018, **226**, 441–450.
- 25 A. Han, J. Sun, H. Zhang, G. K. Chuah and S. Jaenicke, *ChemCatChem*, 2019, **11**, 6425–6430.
- 26 X. Lan, N. Huang, J. Wang and T. Wang, *Chem. Commun.*, 2018, **54**, 584–587.
- 27 Z. Zhu, C. Ma, K. Yu, Z. Lu, Z. Liu, P. Huo, X. Tang and Y. Yan, *Appl. Catal., B*, 2020, **268**, 118432.
- 28 P. Bai, X. Tong, J. Wan, Y. Gao and S. Xue, *J. Catal.*, 2019, **374**, 257–265.
- 29 J. Xue, X. Li, S. Ma, P. Xu, M. Wang and Z. Ye, *J. Mater. Sci.*, 2018, **54**, 1275–1290.
- 30 W. Hou, H. Xu, Y. Cai, Z. Zou, D. Li and D. Xia, *Appl. Surf. Sci.*, 2020, **530**, 147218.
- 31 W. Dai, J. Yu, S. Luo, X. Hu, L. Yang, S. Zhang, B. Li, X. Luo and J. Zou, *Chem. Eng. J.*, 2020, **389**, 123430.
- 32 Y. Chen, Y. Zhou, Q. Dong and H. Ding, *CrystEngComm*, 2018, **20**, 7838–7850.
- 33 H. Huang, X. Li, J. Wang, F. Dong, P. K. Chu, T. Zhang and Y. Zhang, *ACS Catal.*, 2015, **5**, 4094–4103.
- 34 H. Zhao, X. Liu, Y. Dong, Y. Xia, H. Wang and X. Zhu, *ACS Appl. Mater. Interfaces*, 2020, **12**, 31532–31541.
- 35 Y. Xiong, S. Chen, F. Ye, L. Su, C. Zhang, S. Shen and S. Zhao, *Chem. Commun.*, 2015, **51**, 4635–4638.
- 36 D. Zhao and C. Cai, *Dyes Pigm.*, 2021, **185**, 108957.
- 37 C. C. Wang, M. Liu, B. Y. Man, C. S. Chen, S. Z. Jiang, S. Y. Yang, X. G. Gao, S. C. Xu, B. Hu, Z. C. Sun, J. J. Guo and J. Hou, *AIP Adv.*, 2012, **2**, 012182.
- 38 X. Meng, C. Zhang, C. Dong, W. Sun, D. Ji and Y. Ding, *Chem. Eng. J.*, 2020, **389**, 108957.
- 39 M. Kotal, A. Sharma, S. Jakhar, V. Mishra, S. Roy, S. C. Sahoo, H. K. Sharma and S. K. Mehta, *Cryst. Growth Des.*, 2020, **20**, 4627–4639.
- 40 S. Rohani, A. Ziarati, G. M. Ziarani, A. Badieli and T. Burgi, *Catal. Sci. Technol.*, 2019, **9**, 3820–3827.
- 41 J. Chakraborty, I. Nath and F. Verpoort, *Chem. Eng. J.*, 2019, **358**, 580–588.
- 42 P. Chen, H. Liu, Y. Sun, J. Li, W. Cui, L. A. Wang, W. Zhang, X. Yuan, Z. Wang, Y. Zhang and F. Dong, *Appl. Catal., B*, 2020, **264**, 118545.
- 43 X. Zhang, G. Li, C. Fan, G. Ding, Y. Wang and P. Han, *Comput. Mater. Sci.*, 2014, **95**, 113–120.
- 44 Z. Qiang, X. Liu, F. Li, T. Li, M. Zhang, H. Singh, M. Huttula and W. Cao, *Chem. Eng. J.*, 2021, **403**, 126327.
- 45 Z. Zhao, Y. Zhou, F. Wang, K. Zhang, S. Yu and K. Cao, *ACS Appl. Mater. Interfaces*, 2014, **7**, 730–737.
- 46 J. Jiang, K. Zhao, X. Xiao and L. Zhang, *J. Am. Chem. Soc.*, 2012, **134**, 4473–4476.
- 47 L. Ye, L. Zan, L. Tian, T. Peng and J. Zhang, *Chem. Commun.*, 2011, **47**, 6951–6953.
- 48 R. Zhang, Q. Wang, J. Liang, Q. Li, J. Dai and W. Li, *Phys. B*, 2012, **407**, 2709–2715.
- 49 Y.-N. Gong, W. Zhong, Y. Li, Y. Qiu, L. Zheng, J. Jiang and H.-L. Jiang, *J. Am. Chem. Soc.*, 2020, **142**, 16723–16731.
- 50 J. Li, X. Wu, Z. Wan, H. Chen and G. Zhang, *Appl. Catal., B*, 2019, **243**, 667–677.
- 51 G. Zhou, Z. Tian, H. Sun, J. Zhang, H. Zhao, P. Li and H. Sun, *J. Phys. Chem. Solids*, 2020, **146**, 109577.
- 52 P. K. Prajapati, S. Saini and S. L. Jain, *J. Mater. Chem. A*, 2020, **8**, 5246–5254.
- 53 W. Fu, X. Xu, W. Wang, J. Shen and M. Ye, *ACS Sustainable Chem. Eng.*, 2018, **6**, 8935–8944.